Computational Insights into Electrolyte-Dependent Li-ion Charge-Transfer Kinetics at the Li_xCoO_2 Interface

Joakim Halldin Stenlid[1,†*], Pjotrs Žguns[2], Daniele Vivona[3], Abhishek Aggarwal[2][4], Kiarash Gordiz[4], Yirui Zhang[3][4], Shakul Pathak[5], Martin Z. Bazant[5][6], Yang Shao-Horn[2][3][4], Artem Baskin[1], and John W. Lawson[7]*

[1] KBR, Inc., Intelligent Systems Division, NASA Ames Research Center, Moffett Field, California 94035, United States
[2] Department of Materials Science and Engineering, Massachusetts Institute of Technology, 77 Massachusetts Avenue, Cambridge, Massachusetts 02139, United States
[3] Department of Mechanical Engineering, Massachusetts Institute of Technology, 77 Massachusetts Ave., Cambridge, MA 02139, United States
[4] Research Laboratory of Electronics, Massachusetts Institute of Technology, 77 Massachusetts Avenue, Cambridge, Massachusetts 02139, United States
[5] Department of Chemical Engineering, Massachusetts Institute of Technology, Cambridge, Massachusetts 02142, United States
[6] Department of Mathematics, Massachusetts Institute of Technology, Cambridge, Massachusetts 02142, United States
[7] Intelligent Systems Division, NASA Ames Research Center, Moffett Field, California 94035, United States

KEYWORDS: Interface charge-transfer kinetics; Coupled ion-electron transfer; Li-ion batteries; Constrained density functional theory; Constant potential calculations.

ABSTRACT: Interface engineering remains a largely underexplored area and yet it holds the keys to high performance Li-ion batteries. It is the charge transfer across electrode-electrolyte interfaces, its inefficient energetics and sluggish kinetics that are oftentimes significant obstacles for achieving fast charging and high power regimes without compromising battery lifespan. This work propose a Boltzmann-averaged first principles workflow based on constant potential and constrained density functional theory for estimation of atomic scale factors influencing coupled ion-electron charge transfer kinetics across battery electrode-electrolyte interfaces. The approach estimates diabatic Li^+ interface energy landscapes as function of the interface character and operational conditions, needed to simulate charging/discharging currents. Experimental trends for the Li_xCoO_2 ($0.5 \leq x \leq 1.0$) electrode in varied organic electrolytes with $LiPF_6$ and $LiClO_4$ salts are reproduced, identifying Li^+ transfer energy and Li^+ adsorption energy as decisive factors influencing the enhanced kinetics in $LiClO_4$-based electrolytes over $LiPF_6$, rationalized by a stronger surface interaction of ClO_4^-.

† This work was authored by employees of KBR Wyle Services, LLC under Contract No. 80ARC020D0010 with the National Aeronautics and Space Administration.

High power density and fast charging batteries are instrumental in the transition to electrified aerial, maritime, and terrestrial transportation.[1–4] Charge-transfer across interfaces of battery components plays a critical role in dictating charging/discharging kinetics where suboptimal Li-ion (Li^+) transfer is a significant bottleneck impeding the performance of the battery.[5,6] This *interface challenge* pertains to both traditional and emerging Li-ion battery chemistries, including liquid[6]- as well as solid[5]-state electrolytes. Although interfacial engineering–via, e.g., advanced electrolyte formulations,[7–10] surface modifications,[7,8,11] and surface coatings[7,8]–has attracted substantial interest in the battery community in recent years,[7–11] it remains a relatively underexplored area in the pursuit of rational battery design. Thus, enhancing the atomic- to macrolevel understanding of the interplay between electrode materials and electrolytes can provide guidance towards improved performance and lifespan of batteries.

Theoretical modeling offers a gauge to identify the role of atomic-scale factors in controlling observable charging/discharging rates and, thus, enables formulation of fundamental engineering principles.[12–14] Butler-Volmer (BV)[15–17] theory has traditionally been used to model interface charge transfer kinetics, where the classical physics-based BV is considered to reflect cases where ion transfer (IT) steps are rate limiting. In contrast, the influence of electron transfer (ET) on charge transfer kinetics, as described by Marcus-Hush-Chidsey (MHC)[18–23] theory, has lately been highlighted for both Li^+ intercalation[24–27] as well as conversion[28] electrodes. In the more general case, mixed IT and ET rate control can be expected, motivating the recently introduced theory of coupled ion-electron transfer (CIET).[14,29] In CIET, IT and ET are assumed to occur simultaneously along a shared reaction coordinate,[14,29] where the description of IT in the classical rather than quantum regime distinguishing CIET from the related theory of coupled proton-electron transfer (CPET).[30–33] Similar to BV- and MHC-based approaches, the parameters needed for CIET can be directly evaluated from atomistic and first principles modeling, including solvent reorganization energy (λ), electronic coupling (H_{DA}) between donor and acceptor states, as well as ion adsorption (ω_{Li^+}) and ion transfer (β) energies. While the dynamic nature of the interfaces can be captured using enhanced sampling molecular dynamics (MD) techniques,[34,35] the CIET parameters are derived from first principles calculations conducted at constant charge states in order to probe the free energy landscape before and after charge transfer–accessible via, e.g., constrained density functional theory (cDFT).[36] In addition, to reflect experimental conditions and to minimize the influence of finite cell-size effects, the calculations should be carried out at constant electrode potential (i.e., constant electron chemical potential or Fermi level), which can be achieved via electrochemistry-adapted DFT using, e.g., grand canonical potential approaches.[37] The CIET theory, hence, outlines a generally applicable framework that links atomic scale properties to battery performance, allowing for independent first principles evaluation of experimentally derived data as well as for in silico-guided materials design.

In this work, we develop a computational workflow based on CIET theory combined with constrained and constant potential DFT (**Scheme 1**) for analysis of the electronic and molecular properties that influence the IT and

ET contributions to interface charge transfer resistance. The modeling approach complements previous efforts that sample the free energy landscape of battery interfaces using classical MD simulations, which focused on IT but neglects ET.[35,38] The approach also extends on earlier first-principles work on battery interface kinetics by accounting for electrode bias as well as the coupled transfer of ions and electrons.[28,39] By employing constant potential DFT, the approach ensures that the reaction landscape is explored under equal conditions as the addition/removal of ions from a finite model surface otherwise gives rise to spurious fluctuations of the electron chemical potential, associated with noisy or biased results.[40] Recent work on the $LiFePO_4$ and $LiCoO_2$ cathodes has, in addition, found that CIET models represents experimental data better than models that only reflect ET or IT.[14,24,25,27,29] From constrained DFT, it is possible to sample the reaction landscape for the reduced and oxidized charge states separately allowing for the evaluation of the diabatic energy profiles needed to obtain the charge-transfer parameters used in CIET. Using our framework, we can thus move closer to simulating realistic battery conditions, including accounting for simultaneous ET and IT, but also by emulating electrode potential, temperature, and ion concentration. The computational approach is benchmarked by reproducing measured current densities[27] at the state-of-the-art[41] Li_xCoO_2 (LCO) electrode at varied states of charge (SOC; $0.5 \leq x \leq 1.0$) and as a function of the composition of a liquid organic electrolytes based on ethylene carbonate (EC) and ethyl methyl carbonate (EMC) containing $LiPF_6$ and $LiClO_4$ salts. Our work provides insights into critical aspects towards improved interface kinetics, it explains the faster charge transfer kinetics observed in $LiClO_4$ electrolytes in terms of atomic scale properties, and sets the stage for future searches for battery materials with tailored interface properties.

Our computation framework to evaluate exchange current density within CIET framework is outlined in **Scheme 1** and summarized below, with more details available in **Note S1-S2**:

First, to simulate the cathode half-cell, models of the Li_xCoO_2-electrolyte interface with x = {0.50, 0.75, 1.00} are created from the rhombohedral ($R\bar{3}m$) $LiCoO_2$ scaffold structure, i.e., assuming topotactical (de)lithiation. The LCO surface is represented by a periodic (1, 2/3; 0, 4) supercell model of the $(10\bar{1}4)$ facet, which is a commonly observed[42] and low energy[43] surface. $(10\bar{1}4)$ exposes Li-ion transport channels[43–45] that can exchange Li^+ with the electrolyte (illustrated in **Scheme 1**). Consistent with early battery cycles,[46–48] a pristine interface without a cathode-electrolyte interphase layer is considered. Electrolyte microenvironments are sampled as different adsorption structures. Leveraging our recent free energy molecular dynamics simulations on LCO$(10\bar{1}4)$ interfaced with EC/EMC (3:7) electrolytes,[38] we extract local interface adsorption complexes of Li^+ coordinated to different numbers of electrolyte molecules and counterions (PF_6^- and ClO_4^-) spanning a total coordination number (CN) of 3-6 and an anion CN (CN_{anion}) of 0-2. Approximately 40 adsorption structure are sampled for every combination of SOC and

Li-salt. Input parameters to the CIET model are thereafter computed for each adsorption state as described below.

Second, charge transfer properties (*vide infra*) associated with the interface models are computed using constrained DFT (cDFT)[49–51] to ensure that the charge state is fixed at the LCO interface. cDFT is combined with constant potential DFT,[37] where the electrode potential corresponds to the reversible potential (i.e., the open circuit voltage, OCV, when referenced to Li/Li^+)[52] of the LCO half-cell at the given SOC. A graphene layer beneath the surface slab model acts as electron reservoir[36] (i.e., a computational charge collector), ensuring a continuous variation of the Fermi level (and thereby the potential) of the cell as electrons are added or subtracted. Using the constant potential scheme, the free energy landscape can be sampled at the same conditions facilitating fair comparison between states. Unless otherwise specified, these calculations are carried out in VASP[53,54] (version 6.3.2) using the PBE-D3(BJ) level of theory[55–57] and standard PAW[58,59] core potentials. To account for both directional and long-range solvation effects, hybrid explicit-implicit solvation models[60,61] are employed with the implicit part represented by VASPsol[60,61] using a dielectric constant of 20 corresponding to a 3:7 EC/EMC mixture.[62]

Third, to evaluate the electrode current density (i^{CIET}) at varied interface properties and overpotential, η_f ($\tilde{\eta}_f = \frac{e\eta_f}{k_B T}$), the computed charge transfer properties are inputted into the CIET[14] model (details in **Note S2**). The electron-coupled ion transfer version of CIET,[14] described by eq. 1-2, is found to best fit experimental data[27] and therefore used herein.

$$i^{CIET} = i^* \left(\frac{\tilde{c}_O(\omega_{Li^+})}{1+\mathrm{e}^{\tilde{\eta}_f}} - \frac{\tilde{c}_R}{1+\mathrm{e}^{-\tilde{\eta}_f}} \right) \mathrm{erfc}\left(\frac{\tilde{\lambda} - \sqrt{1+\sqrt{\tilde{\lambda}}+\tilde{\eta}_f^2}}{2\sqrt{\tilde{\lambda}}} \right) \quad \text{(eq. 1)}$$

$$i^* = \frac{e\Delta_e(H_{\mathrm{DA}}^2)}{h} \frac{1}{A_S} \frac{\mathrm{e}^{-\Delta\tilde{G}_{\ddagger}^{IT}(\Delta E^{IT})}}{\gamma_{\ddagger}^{IT}} \quad \text{(eq. 2)}$$

Above, h is the Planck constant and overline "~" indicating dimensionless variables normalized by the thermal energy ($\mathrm{k_B}T$) or bulk concentrations. Some parameters are given by the ambient conditions, the material of choice, as well as the electrolyte composition. These include: the temperature (T); Li-ion concentration in LCO (c_R) and the electrolyte (c_O); as well as the area of a reaction site (A_S). Other properties are difficult or impossible to directly obtain from experiments, although they can be estimated by fitting procedures to, e.g., Tafel plots. Alternatively, the properties can be predicted through, e.g., the proposed computational workflow. These computed properties are: the adsorption energy of Li^+ ($\omega_{\mathrm{Li^+}}$); the ion transfer energy (β) over the reaction coordinate at a constant charge state (q), which also determines the IT reaction barrier $\Delta G_{\ddagger}^{IT}$; the solvent reorganization energy (λ); as well as the electronic coupling matrix element (H_{DA}^2). The latter is proportional to the electron chemisorption energy, Δ_e. **Note S1-S2** provides a comprehensive overview of the computation of these charge transfer properties.

The above modeling framework provides the connection needed between atomic scale properties of electrode-electrolyte interfaces and current densities, relating directly to battery power and charging performance. In the following, the computational workflow is used to gain insights into the charge transfer kinetics of the LCO cathode in varied electrolytes, identifying the key atomic factors controlling fast interface kinetics.

By simulating $Li^{-/0/+}$ vacancies at the LCO interface (**Scheme 1A**), we find that, under OCV, neutral Li vacancies are preferentially formed (i.e., Li^++e^- leaves simultaneously) for all considered SOC (**Figure S8**). In addition, the relative chemical potential of Li (Li^++e^-), $\mu_{Li^+ + e^-} = \mu_{Li}$, at the interface compared to bulk LCO is 0.10, 0.11 and 0.22 eV for x = 0.50, 0.75, and 1.00, respectively, meaning that surface vacancies are preferred over bulk (**Figure 1.A**). In contrast, the first subsurface layer Li has approximately the same μ_{Li} as the bulk. By analyzing the site-projected DOS (**Figure S4-S6**) of the Li 2*s* band for Li^+ at the interface versus bulk LCO, it is found that the band center (ε_{Li2s}) for surface Li^+ is higher compared to bulk, indicating a lower filing of bonding electronic states and, thus, weaker surface O-Li bonds (**Figure 1.B**). On the other hand, the subsurface Li^+ shows almost no difference in the Li 2*s* band center compared to bulk Li^+, explaining their stability. The ε_{Li2s} results correlate with shifts in the O 2*p* states (ε_{O2p}) towards the Fermi level for surface O compared to bulk (**Figure 1.C**). Such shifts in ε_{O2p} have been used to explain ion intercalation in terms of a reduced penalty for charge transfer associated with the upshift in ε_{O2p} at the surface versus bulk due to a smaller O 2*s*-Co 3*d* band gap (**Figure S7**).[63] In brief, the Li vacancy results showcase that a lower concentration of Li^+ is expected at the interface compared to the bulk at OCV, but also that desorption/adsorption of Li^+ from/to the LCO surface is accompanied by oxidation/reduction of interface $Co^{3+/4+}$, corroborating the hypothesis of a coupled electron-ion mechanism of Li^+ transfer.

CIET barriers are computed for the cathode-electrolyte interface during charging/discharging following the steps outlined in **Figure 2.A**, where barriers are associated with both IT and ET steps (**Scheme 1.B)**. At the reversible potential of LCO (OCVs of 4.20, 3.95, 3.05 V versus Li/Li^+ for LCO at SOC x=0.50, 0.75, 1.00)[52], the intercalation/de-intercalation equilibrium reads:

$$Li^+(solv) + e^- + Co^{4+}(@LCO) \rightleftharpoons Li^+\text{-}Co^{3+}(@LCO) \qquad \text{(eq. 3)}$$

The free energy profile of the Li^+ deintercalation reaction in **Figure 2.B** shows detailed steps where Li^+ is first in a LCO bulk intercalation state (① in **Figure 2.A**). Li^+ then transitions via a surface state (② in **Figure 2.A**), before reaching a Li^+ solvation complex at the outer Helmholtz plane (OHP, ③ in **Figure 2.A**) of the electric double layer. Ultimately Li^+ ends in the bulk electrolyte (④ in **Figure 2.A**). ET (coupled to IT) occurs in the step ② ⇌ ③. This step is assumed to be the rate-limiting step based on previous experimental and MD studies.[27,38] Within the hypothesis of electron-coupled Li^+ transfer, we evaluate the barrier by computing two separate IT energy desorption profiles for the step ② ⇌ ③ at constant charge states, q, corresponding to a reduced (q=q_R, i.e., Co^{3+}) versus

oxidized (q=q_O, i.e., Co^{4+}) surface, respectively. Estimating the coupling ($\propto H_{DA}$) and reorganization energy (λ) for ET between the q_O and q_R states along the IT desorption profiles provides the reaction barrier for each IT coordinate (ξ), with the minimal energy path corresponding to the most likely reaction pathway (red path in **Scheme 1.C**). Herein, the IT desorption profiles are computed using cDFT. An example is shown in **Figure 2.C** demonstrating that Li^+ desorption is endothermic at q_R and exothermic at q_O. These diabatic desorption profiles from ② ⇌ ③ are found to be weakly sigmoidal but can, in order to simplify the implementation of a CIET model,[14,29] be approximated as linear with resulting R^2 values of 0.90-0.95. Comparing the estimated free energy rection profiles and barriers along the joint ET-IT reaction coordinate holds the key to evaluating the variation in charge-transfer reaction kinetics from one interface to another.

To reflect the dynamic nature of the interface, different interfacial Li^+-solvation configurations are sampled from recent MD simulations[38] to assess the average influence of the local coordination environments to the overall current density, revealing that the lowest energy adsorption complexes correspond to a total CN of 4-5 with CN_{anion} of 0-1 and coordination to EC being slightly preferred over EMC, in agreement with the results of Aggarwal et al.[38] For each adsorption state, ω_{Li^+} is computed from a thermochemical cycle referenced to the average μ_{Li^+} of the bulk electrolyte (**Note S1.3** and **Scheme S1**). As seen in **Figure 3.A**, these low-energy complexes yield weakly endergonic Li^+ free energies of adsorption (ω_{Li^+}) in a narrow spread around 11 and 20 meV for ClO_4^- and PF_6^-. One key difference between ClO_4^- and PF_6^- relates to the bulk electrolyte reference state, with ClO_4^- corresponding to a less favorable bulk solvation. Another important distinction between ClO_4^- and PF_6^- is the interplay between the anions and LCO (*vide infra*). For 3 > CN > 5 and CN_{anion} > 1, ω_{Li^+} is generally > 100 meV, hence these structures are less probable and are found to have a small influence on the interface kinetics at typical operational temperatures (~300 K). Using the relative ω_{Li^+} values coming from different Li^+-coordination complexes we can model the thermally-weighted CIET current density contribution from each adsorption state, and compute a total representative interface current via Boltzmann-averaging (with $\mathbf{p}_j$=$\mathbf{p}_j[\omega_{Li^+}, \beta, \lambda, H_{DA}]$ below, and Z representing the partition function estimated from the sampled states):

$$i_{tot} = \langle i \rangle = \frac{1}{Z}\sum_j i_j^{\mathrm{CIET}}(\mathbf{p}_j)\, exp\left(\frac{-\Delta\omega_{Li^+,j}}{k_B T}\right) \qquad \text{(eq. 3)}$$

The IT between the LCO surface and the OHP of the electrolyte encompasses the desolvation/solvation process of Li^+ and the ion transfer energy, β, is sensitive to the character and charge state of the electrode as well the electrolyte microenvironment at the interface (**Figure 3B**). Three results related to β will be highlighted. First, it is found that the reaction is approximately symmetric (i.e., $\beta \approx \beta_O(q = q_O) \approx \beta_R(q = q_R)$, and $\alpha \approx 0.5$) for the low-energy adsorption states. This is reasonable at OCV conditions given the small deviation from equilibrium μ (**Figure 2.B**), and the revealed reaction symmetry in agreement with the experimentally determined value of α=0.48 for $Li_{0.5}CoO_2$

in $LiPF_6$ and carbonate electrolyte.[64] Second, one can estimate the IT-related reaction activation barrier, $\Delta G_{\ddagger}^{IT}$, from the β using eq. S12 resulting in $\Delta G_{\ddagger}^{IT}$ values of 0.45 to 0.52 eV. These are close to the ~0.5 eV estimated by Yamada *et al.*[65] using electrochemical impedance spectroscopy for 0.5 M $LiClO_4$ salts in propylene carbonate. Last, **Figure 3.B** presents a clear trend when comparing $LiClO_4$ and $LiPF_6$ salts, revealing a slightly decreased β and associated lowered barrier in $LiClO_4$ electrolytes, which is in agreement with MD-simulated Li^+ IT energies using classical forcefields at constant charge state.[38]

To estimate the influence of ET on the charge transfer kinetics, average reorganization energies, λ, of ~109 and ~102 meV are computed for the PF_6^- and ClO_4^- electrolytes, respectively–a small but not insignificant difference (*vide infra*). λ together with the electronic coupling (H_{DA}) are the important interface properties for the ET part of CIET. λ can be estimated for each IT coordinate (ξ in **Scheme 1**) by exploring pairs of Marcus parabolas (one each for the q_{O} and q_{R} states) that describe the change in chemical potential along the ET coordinate (χ in **Scheme 1**), with details in **Note S1.2**. The λ values are estimated from the vertical energy difference when changing the charge state at the local energy minimum for the opposite charge state and obtained from the average value for the q_{O} and q_{R} states. Values reported in **Figure 3.C** correspond to the λ of the transition state IT coordinate. λ encompasses contributions from both the LCO and electrolyte parts of the interface. Regardless, the average λ values are close to the 90 meV estimated for bulk LCO (**Note S9**) as well as the 115 meV extracted from current-voltage response experiments for LCO.[27] Hence, one can conclude that the solvent effect on λ is small, both absolute and relative numbers. However, in contrast to the SOC–for which λ is almost insensitive–the minor variation in λ with the electrolyte composition has some influences on the relative current densities as discussed towards the end of this letter.

The other critical parameter determining the rate of ET, i.e. the electronic coupling (H_{DA}) between the electron donor and acceptor states at the interface, shows no significance sensitive to the electrolyte but some dependence on the SOC of LCO. H_{DA} is herein computed using the approach of Van Voorhis and coworkers,[49–51] as implemented[36] in the GPAW modeling package.[66,67] Upon Li^+ interface adsorption (i.e., surface intercalation), Co^{4+} at the LCO (x=0.5) surface is nominally reduced to Co^{3+} as indicated by a small polaron localizing at around the CoO_6 octahedra (see insert of **Figure 2.C**). For SOC $0.5 \leq x \leq 0.75$, bulk LCO is metallic (computationally and experimentally[68,69]) and electron transfer occurs from a delocalized subsurface to the bound surface state. Interestingly, the electrolyte has no significant influence on the electronic coupling and the computed H_{DA} for PF_6^- and ClO_4^- is close to 35 meV regardless of adsorption state for $0.5 \leq x \leq 0.75$. A clear down shift to an average H_{DA} of ~22 meV is, however, seen as SOC changes to x=1.00. This change originates in the metal to semi-conductor phase transition of bulk LCO, which is experimentally known to occur over a biphase region at $0.77 < x < 0.94$,[68,69] that leads to a change in the bulk donor state at $x \approx 1.00$. Hence, H_{DA} plays an important role in modulating the charge

transfer kinetics as the SOC of LCO changes from x=0.50-0.75 to x=1.00, whereas the relative influence of H_{DA} is insignificant when comparing the electrolyte compositions evaluated in this work.

Using the computed interface charge transfer parameters in **Figure 3** combined with the Boltzmann-weighted CIET formula in eq. 3, the computed current density, i, of the LCO electrodes is estimated as a function of the electrolyte character and the SOC of LCO (**Figure 4**). Remarkable agreements are found compared to experimentally reported polarization curves from Zhang *et al*.[27] The correspondence is good to excellent (within an order of magnitude). Experimentally, an increased state of charge of LCO generally yields higher i while ClO_4^--based electrolytes outperforms PF_6^-, which are correctly reproduced by our simulated trends using the DFT-computed parameters. These results corroborates that the computational framework outlined in this work is able to make predictions about the macroscopic effects on electrode kinetics from variations in molecular level details of a battery electrolyte and electrode, which is further discussed in the following.

The simulated trends shown in **Figure 4** can be rationalized by the favorable characteristics (large H_{DA} and/or small β, λ, or ω_{Li^+}) of those individual interface adsorption states that give the largest overall contribution to the current density. The sensitivity analysis in **Figure S2** of all parameters entering in the CIET model indicate that the current density from a given adsorption state has a particular dependency on changes in $H_{DA} > \beta \approx \lambda > \omega_{Li^+}$, when varied within moderate bounds around the values corresponding to the most favorable state of the $Li_{0.5}CoO_2$ interfaces with the ClO_4^- electrolyte. In addition to this *intrinsic rate* of a given surface adsorption state, the influence of each state to the total reaction rate is weighted by its probability as evaluated by the relative value of ω_{Li^+}, hence giving the ω_{Li^+} property an added importance. Recall that, whereas H_{DA} is mainly affected by the SOC and insensitive to the electrolyte, β, λ, and ω_{Li^+} show electrolyte-dependency to some degree, hence all adsorbate states that give large contributions to the current density are associated with low values of ω_{Li^+}, β and λ. Of these structures, complexes containing anions (ClO_4^- or PF_6^-) with CN_{anion}=1 dominate. The results, moreover, suggest that a key underlying origin to the difference between ClO_4^- or PF_6^- is the more pronounced interaction of ClO_4^- with the LCO surface; this yields a more beneficial adsorption of Li^+ at the OHP associated with a closer adsorption distance (~0.1 Å). The surface interactions of ClO_4^- is also associated with an additional stabilization of the surface and electrolyte during Li^+ solvation and desolvation that primarily affects the β, which is significantly more beneficial (i.e., smaller) for ClO_4^-. In addition, the less favorable bulk μ_{Li^+} in the ClO_4^- electrolyte compared to PF_6^- yields a more favorable ω_{Li^+} at the interface for the case of ClO_4^-, which has been previously explained by Aggarwal et al.[38] Although the bulk electrolyte effect, as well as influence of the LCO interaction difference of ClO_4^- compared to PF_6^-, are weak to moderate, they are significant enough to alter the current density by an order of magnitude when adding up the contributions of β, λ, and ω_{Li^+}, with β defining the major part of the difference between the electrolytes.

Regarding the variation in the current density with the SOC of LCO, the simulated current densities follow experimental variations closely. The CIET model includes a dependency on the Li^+ concentration in LCO, which is the main factor contributing to the current density shift with SOC of $0.5 < x < 0.8$ for Li_xCoO_2. However, as the SOC approaches full discharge, i.e., $x \approx 1.00$, the current density of LCO is known to drop considerably.[41] This is reflected by our simulations showing a 3-4 order of magnitude current density decrease for x=1.00 compared to x=0.50 (**Figure S11**), which is primarily a consequence of the change in the H_{DA} with SOC (**Figure 3.D**).

Our work, focused on the $LiCoO_2$ intercalation-type cathode, suggests that the most influential atomic level features for enhanced interface kinetics pertains to ET properties of the electrode material surface and IT properties of the electrolyte. Surface engineering yielding stronger coupling, H_{DA}, between electronic donor and acceptor states through, e.g., promotion of certain surface facets, doping, or coating outlines promising avenues for improvement. Of promise is, similarly, electrolyte design that tune the balance in the interaction of Li^+ with the electrolyte as well as the electrode surface providing a flat free energy landscape for Li^+ transfer with small β, and ω_{Li^+}. This work corroborate contemporary strategies in fast charging and high power battery design, but dresses the materials guidelines in an atomistic outfit aiming to benefit the nanoscale tailoring of battery material interfaces with improved charge transfer kinetics.

The modeling framework employed in this work offer a direct tool to assess charge transfer kinetics at electrode interfaces. This approach lends itself well to rationalization, finetuning, or testing of a limited selection of battery systems where refined understanding is required. However, the large computational overhead of the DFT methods prohibits high-throughput studies, why future work will target development of faster approximative methods to enable screening for improved battery components. In this direction, a few promising descriptors correlating with the λ, ω_{Li^+}, β, and H_{DA} charge transfer properties are highlighted below: first, λ is known to correlate with the static and optical dielectric constants of the medium;[70,71] second, the electrostatic potential (ESP),[72–74] oxygen/lithium pDOS centers,[63,75] charge population analysis,[76] and the Crystal Orbital Hamilton Population (COHP)[76,77] are promising for estimations of β; and, third, ω_{Li^+} could be evaluated from solvation or ion-pairing energies.[78,79] Last, estimating H_{DA} is challenging, but positive results based on neural network models have been shown for molecular systems based on atomic orbital overlap and geometric descriptors.[80] In brief, future studies are encouraged to evaluate the herein employed charge-transfer property descriptors λ, ω_{Li^+}, β, and H_{DA} through computationally efficient physics-derived or machine-learning/data-driven surrogate models.[81–83]

In summary, this study introduces and employs a computational workflow based on coupled ion-electron theory (CIET) of interface charge transfer. It is used to simulate the charging and discharging processes at Li_xCoO_2-liquid EC/EMC electrolyte interfaces using charge transfer kinetic parameters derived from constrained and constant potential density functional theory (DFT) calculations. The simulations closely replicate experimental rate trends,

indicating a notable preference for electrolytes containing the $LiClO_4$ salt over $LiPF_6$, commonly used in commercial batteries. This preference is rationalized through the interplay of two factors closely linked to the solvent environment at the interface. First, $LiClO_4$ yields a more favorable adsorption energy (ω_{Li^+}) for Li^+ at the electric double layer of the interface through the more pronounced interaction of ClO_4^- with the Li_xCoO_2 surface compared to PF_6^-. Second, the energetics of Li^+ transfer (β) across the interface is more favorable for $LiClO_4$ compared to $LiPF_6$, also a consequence of the slightly stronger interaction of ClO_4^- with the Li_xCoO_2 surface and the shorter ClO_4^--binding distance. Based on our findings, our proposed workflow outlines a computational strategy to independently estimate charge transfer kinetics to gain atomic scale insight about the factors governing fast charge transfer and for the development of design guidelines for materials interfaces with enhanced power and charging performance in battery applications.

ASSOCIATED CONTENT

Supporting Information

The Supporting Information is available free of charge.

Computational and modeling details; parameter sensitivity analysis CIET simulations; density of states plots; Li vacancy formation energies; polarization curve at x=1.00; reorganization energy analysis. (PDF)

AUTHOR INFORMATION

Corresponding Author

* joakim.halldin.stenlid@nasa.gov (JHS) and john.w.lawson@nasa.gov (JWL)

Author Contributions

The manuscript was written through contributions of all authors. All authors have given approval to the final version of the manuscript. JHS conceived the research, performed the calculations, analyzed the data, and wrote the manuscript; PZ, AA, KG, DV, YZ, SP, MZB, YS-H, JWL, and AB analyzed the data and gave feedback on the manuscript; JWL supervised the research and obtained financial support.

ACKNOWLEDGMENT

This work was supported by funding from the Transformative Tools and Technologies (TTT) project of the Aeronautics Research Mission Directorate (ARMD) at the National Aeronautics and Space Administration (NASA). P.Z., D.V., A.A., K.G., and Y.S.-H. acknowledge support from NASA Grant Number 80NSSC21M0108. Additional support was provided by Shell International Exploration & Production Inc. (Y.Z., S.P., M.Z.B., Y.S.-H.). Computational resources supporting this work were provided by the NASA High-End Computing (HEC) program through the NASA Advanced Supercomputing (NAS) division at Ames Research Center.

REFERENCES

(1) Ahmad, F.; Khalid, M.; Panigrahi, B. K. Development in Energy Storage System for Electric Transportation: A Comprehensive Review. *J. Energy Storage* **2021**, *43*, 103153.

(2) Olabi, A. G.; Abbas, Q.; Shinde, P. A.; Abdelkareem, M. A. Rechargeable Batteries: Technological Advancement, Challenges, Current and Emerging Applications. *Energy* **2023**, *266*, 126408.

(3) Viswanathan, V.; Epstein, A. H.; Chiang, Y.-M.; Takeuchi, E.; Bradley, M.; Langford, J.; Winter, M. The Challenges and Opportunities of Battery-Powered Flight. *Nature* **2022**, *601*, 519–525.

(4) Adu-Gyamfi, B. A.; Good, C. Electric Aviation: A Review of Concepts and Enabling Technologies. *Transp. Eng.* **2022**, *9*, 100134.

(5) Yu, C.; Ganapathy, S.; Eck, E. R. H. van; Wang, H.; Basak, S.; Li, Z.; Wagemaker, M. Accessing the Bottleneck in All-Solid State Batteries, Lithium-Ion Transport over the Solid-Electrolyte-Electrode Interface. *Nat Commun* **2017**, *8*, 1086.

(6) Kondo, Y.; Abe, T.; Yamada, Y. Kinetics of Interfacial Ion Transfer in Lithium-Ion Batteries: Mechanism Understanding and Improvement Strategies. *ACS Appl. Mater. Interfaces* **2022**, *14*, 22706–22718.

(7) Aurbach, D.; Markovsky, B.; Salitra, G.; Markevich, E.; Talyossef, Y.; Koltypin, M.; Nazar, L.; Ellis, B.; Kovacheva, D. Review on Electrode–Electrolyte Solution Interactions, Related to Cathode Materials for Li-Ion Batteries. *J. Power Sources* **2007**, *165*, 491–499.

(8) Wright, D. R.; Garcia-Araez, N.; Owen, J. R. Review on High Temperature Secondary Li-Ion Batteries. *Energy Procedia* **2018**, *151*, 174–181.

(9) Zou, Y.; Fu, A.; Zhang, J.; Jiao, T.; Yang, Y.; Zheng, J. Stabilizing the $LiCoO_2$ Interface at High Voltage with an Electrolyte Additive 2,4,6-Tris(4-Fluorophenyl)Boroxin. *ACS Sustainable Chem. Eng.* **2021**, *9*, 15042–15052.

(10) Sun, Z.; Li, F.; Ding, J.; Lin, Z.; Xu, M.; Zhu, M.; Liu, J. High-Voltage and High-Temperature $LiCoO_2$ Operation via the Electrolyte Additive of Electron-Defect Boron Compounds. *ACS Energy Lett.* **2023**, *8*, 2478–2487.

(11) Yang, X.; Lin, M.; Zheng, G.; Wu, J.; Wang, X.; Ren, F.; Zhang, W.; Liao, Y.; Zhao, W.; Zhang, Z.; Xu, N.; Yang, W.; Yang, Y. Enabling Stable High-Voltage $LiCoO_2$ Operation by Using Synergetic Interfacial Modification Strategy. *Adv. Funct. Mater.* **2020**, *30*, 2004664.

(12) A. Franco, A. Multiscale Modelling and Numerical Simulation of Rechargeable Lithium Ion Batteries: Concepts, Methods and Challenges. *RSC Advances* **2013**, *3*, 13027–13058.

(13) Zhang, C.; Cheng, J.; Chen, Y.; Chan, M. K. Y.; Cai, Q.; Carvalho, R. P.; Marchiori, C. F. N.; Brandell, D.; Araujo, C. M.; Chen, M.; Ji, X.; Feng, G.; Goloviznina, K.; Serva, A.; Salanne, M.; Mandai, T.; Hosaka, T.;

Alhanash, M.; Johansson, P.; Qiu, Y.-Z.; Xiao, H.; Eikerling, M.; Jinnouchi, R.; Melander, M. M.; Kastlunger, G.; Bouzid, A.; Pasquarello, A.; Shin, S.-J.; Kim, M. M.; Kim, H.; Schwarz, K.; Sundararaman, R. 2023 Roadmap on Molecular Modelling of Electrochemical Energy Materials. *J. Phys. Energy* **2023**, *5*, 041501.

(14) Bazant, M. Z. Unified Quantum Theory of Electrochemical Kinetics by Coupled Ion-Electron Transfer. *Faraday Discuss.* **2023**, *246*.

(15) Tafel, J. Über die Polarisation bei kathodischer Wasserstoffentwicklung. *Zeitschrift für Physikalische Chemie* **1905**, *50U*, 641–712.

(16) Butler, J. a. V. Studies in Heterogeneous Equilibria. Part III. A Kinetic Theory of Reversible Oxidation Potentials at Inert Electrodes. *Trans. Faraday Soc.* **1924**, *19*, 734–739.

(17) Erdey-Grúz, T.; Volmer, M. Zur Frage der elektrolytischen Metallüberspannung. *Zeitschrift für Physikalische Chemie* **1931**, *157A*, 165–181.

(18) Marcus, R. A. Electrostatic Free Energy and Other Properties of States Having Nonequilibrium Polarization. I. *J. Chem. Phys.* **2004**, *24*, 979–989.

(19) Marcus, R. A. Chemical and Electrochemical Electron-Transfer Theory. *Annual Review of Physical Chemistry* **1964**, *15*, 155–196.

(20) Hush, N. S. Electrode Reactions of the Methyl Halides. *Berichte der Bunsengesellschaft fr Physikalische Chemie* **1957**, *61*, 734–738.

(21) Hush, N. S. Adiabatic Theory of Outer Sphere Electron-Transfer Reactions in Solution. *Trans. Faraday Soc.* **1961**, *57*, 557–580.

(22) Chidsey, C. E. D. Free Energy and Temperature Dependence of Electron Transfer at the Metal-Electrolyte Interface. *Science* **1991**, *251*, 919–922.

(23) Kurchin, R.; Viswanathan, V. Marcus–Hush–Chidsey Kinetics at Electrode–Electrolyte Interfaces. *J. Chem. Phys.* **2020**, *153*, 134706.

(24) Koo, B.; Chung, J.; Kim, J.; Fraggedakis, D.; Seo, S.; Nam, C.; Lee, D.; Han, J.; Jo, S.; Zhao, H.; Nadkarni, N.; Wang, J.; Kim, N.; Weigand, M.; Bazant, M. Z.; Lim, J. Dynamic Surface Phases Controlling Asymmetry of High-Rate Lithiation and Delithiation in Phase-Separating Electrodes. *Energy Environ. Sci.* **2023**, *16*, 3302–3313.

(25) Zhao, H.; Deng, H. D.; Cohen, A. E.; Lim, J.; Li, Y.; Fraggedakis, D.; Jiang, B.; Storey, B. D.; Chueh, W. C.; Braatz, R. D.; Bazant, M. Z. Learning Heterogeneous Reaction Kinetics from X-Ray Videos Pixel by Pixel. *Nature* **2023**, *621*, 289–294.

(26) Bai, P.; Bazant, M. Z. Charge Transfer Kinetics at the Solid–Solid Interface in Porous Electrodes. *Nat. Commun.* **2014**, *5*, 3585.

(27) Zhang, Y.; Fraggedakis, D.; Gao, T.; Pathak, S.; Zhuang, D.; Grosu, C.; Samantaray, Y.; Neto, A. R. C.; Duggirala, S. R.; Huang, B.; Zhu, Y. G.; Giordano, L.; Tatara, R.; Agarwal, H.; Stephens, R. M.; Bazant, M.

Z.; Shao-Horn, Y. Lithium-Ion Intercalation by Coupled Ion-Electron Transfer. ChemRxiv 2024. https://doi.org/10.26434/chemrxiv-2024-d00cp.

(28) Park, H.; Kumar, N.; Melander, M.; Vegge, T.; Garcia Lastra, J. M.; Siegel, D. J. Adiabatic and Nonadiabatic Charge Transport in Li–S Batteries. *Chem. Mater.* **2018**, *30*, 915–928.

(29) Fraggedakis, D.; McEldrew, M.; Smith, R. B.; Krishnan, Y.; Zhang, Y.; Bai, P.; Chueh, W. C.; Shao-Horn, Y.; Bazant, M. Z. Theory of Coupled Ion-Electron Transfer Kinetics. *Electrochim. Acta* **2021**, *367*, 137432.

(30) Warburton, R. E.; Soudackov, A. V.; Hammes-Schiffer, S. Theoretical Modeling of Electrochemical Proton-Coupled Electron Transfer. *Chem. Rev.* **2022**, *122*, 10599–10650.

(31) Melander, M. M. Grand Canonical Rate Theory for Electrochemical and Electrocatalytic Systems I: General Formulation and Proton-Coupled Electron Transfer Reactions. *J. Electrochem. Soc.* **2020**, *167*, 116518.

(32) Li, J.; Stenlid, J. H.; Ludwig, T.; Lamoureux, P. S.; Abild-Pedersen, F. Modeling Potential-Dependent Electrochemical Activation Barriers: Revisiting the Alkaline Hydrogen Evolution Reaction. *J. Am. Chem. Soc.* **2021**, *143*, 19341–19355.

(33) Koper, M. T. M. Theory of the Transition from Sequential to Concerted Electrochemical Proton–Electron Transfer. *Phys. Chem. Chem. Phys.* **2013**, *15*, 1399–1407.

(34) Holoubek, J.; Baskin, A.; Lawson, J. W.; Khemchandani, H.; Pascal, T. A.; Liu, P.; Chen, Z. Predicting the Ion Desolvation Pathway of Lithium Electrolytes and Their Dependence on Chemistry and Temperature. *J. Phys. Chem. Lett.* **2022**, *13*, 4426–4433.

(35) Baskin, A.; Lawson, J. W.; Prendergast, D. Anion-Assisted Delivery of Multivalent Cations to Inert Electrodes. *J. Phys. Chem. Lett.* **2021**, *12*, 4347–4356.

(36) Melander, M.; Jónsson, E. Ö.; Mortensen, J. J.; Vegge, T.; García Lastra, J. M. Implementation of Constrained DFT for Computing Charge Transfer Rates within the Projector Augmented Wave Method. *J. Chem. Theory Comput.* **2016**, *12*, 5367–5378.

(37) Goodpaster, J. D.; Bell, A. T.; Head-Gordon, M. Identification of Possible Pathways for C–C Bond Formation during Electrochemical Reduction of CO_2: New Theoretical Insights from an Improved Electrochemical Model. *J. Phys. Chem. Lett.* **2016**, *7*, 1471–1477.

(38) Aggarwal, A.; Gordiz, K.; Baskin, A.; Vivona, D.; Stenlid, J. H.; Lawson, J. W.; Grossman, J. C.; Shao-Horn, Y. Revealing the Molecular Origin of Driving Forces and Thermodynamic Barriers for Li^+ Ion Transport to Electrode-Electrolyte Interfaces. ChemRxiv, 2024. https://doi.org/10.26434/chemrxiv-2024-hn926.

(39) Zhao, S.; Wang, B.; Zhang, Z.; Zhang, X.; He, S.; Yu, H. First-Principles Computational Insights into Lithium Battery Cathode Materials. *Electrochem. Energy Rev.* **2022**, *5*, 1–31.

(40) Chan, K.; Nørskov, J. K. Electrochemical Barriers Made Simple. *J. Phys. Chem. Lett.* **2015**, *6*, 2663–2668.

(41) Lyu, Y.; Wu, X.; Wang, K.; Feng, Z.; Cheng, T.; Liu, Y.; Wang, M.; Chen, R.; Xu, L.; Zhou, J.; Lu, Y.; Guo, B. An Overview on the Advances of $LiCoO_2$ Cathodes for Lithium-Ion Batteries. *Adv. Energy Mater.* **2021**, *11*, 2000982.

(42) Okubo, M.; Hosono, E.; Kim, J.; Enomoto, M.; Kojima, N.; Kudo, T.; Zhou, H.; Honma, I. Nanosize Effect on High-Rate Li-Ion Intercalation in $LiCoO_2$ Electrode. *J. Am. Chem. Soc.* **2007**, *129*, 7444–7452.

(43) Kramer, D.; Ceder, G. Tailoring the Morphology of $LiCoO_2$: A First Principles Study. *Chem. Mater.* **2009**, *21*, 3799–3809.

(44) Fuller, E. J.; Ashby, D. S.; Polop, C.; Salagre, E.; Bhargava, B.; Song, Y.; Vasco, E.; Sugar, J. D.; Albertus, P.; Menteş, T. O.; Locatelli, A.; Segovia, P.; Gonzalez-Barrio, M. Á.; Mascaraque, A.; Michel, E. G.; Talin, A. A. Imaging Phase Segregation in Nanoscale Li_xCoO_2 Single Particles. *ACS Nano* **2022**, *16*, 16363–16371.

(45) Bates, J. B.; Dudney, N. J.; Neudecker, B. J.; Hart, F. X.; Jun, H. P.; Hackney, S. A. Preferred Orientation of Polycrystalline LiCoO2 Films. *J. Electrochem. Soc.* **2000**, *147*, 59.

(46) Giordano, L.; Østergaard, T. M.; Muy, S.; Yu, Y.; Charles, N.; Kim, S.; Zhang, Y.; Maglia, F.; Jung, R.; Lund, I.; Rossmeisl, J.; Shao-Horn, Y. Ligand-Dependent Energetics for Dehydrogenation: Implications in Li-Ion Battery Electrolyte Stability and Selective Oxidation Catalysis of Hydrogen-Containing Molecules. *Chem. Mater.* **2019**, *31*, 5464–5474.

(47) Zhang, Z.; Yang, J.; Huang, W.; Wang, H.; Zhou, W.; Li, Y.; Li, Y.; Xu, J.; Huang, W.; Chiu, W.; Cui, Y. Cathode-Electrolyte Interphase in Lithium Batteries Revealed by Cryogenic Electron Microscopy. *Matter* **2021**, *4*, 302–312.

(48) Zhang, Y.; Katayama, Y.; Tatara, R.; Giordano, L.; Yu, Y.; Fraggedakis, D.; Guangwen Sun, J.; Maglia, F.; Jung, R.; Z. Bazant, M.; Shao-Horn, Y. Revealing Electrolyte Oxidation via Carbonate Dehydrogenation on Ni-Based Oxides in Li-Ion Batteries by in Situ Fourier Transform Infrared Spectroscopy. *Energy Environ. Sci.* **2020**, *13*, 183–199.

(49) Podloucky, R.; Zeller, R.; Dederichs, P. H. Electronic Structure of Magnetic Impurities Calculated from First Principles. *Phys. Rev. B* **1980**, *22*, 5777–5790.

(50) Wu, Q.; Van Voorhis, T. Extracting Electron Transfer Coupling Elements from Constrained Density Functional Theory. *J. Chem. Phys.* **2006**, *125*, 164105.

(51) Kaduk, B.; Kowalczyk, T.; Van Voorhis, T. Constrained Density Functional Theory. *Chem. Rev.* **2012**, *112*, 321–370.

(52) Guo, M.; Sikha, G.; White, R. E. Single-Particle Model for a Lithium-Ion Cell: Thermal Behavior. *J. Electrochem. Soc.* **2010**, *158*, A122.

(53) Kresse, G.; Furthmüller, J. Efficient Iterative Schemes for Ab Initio Total-Energy Calculations Using a Plane-Wave Basis Set. *Phys. Rev. B* **1996**, *54*, 11169–11186.

(54) Kresse, G.; Hafner, J. Ab Initio Molecular Dynamics for Liquid Metals. *Phys. Rev. B* **1993**, *47*, 558–561.

(55) Perdew, J. P.; Burke, K.; Ernzerhof, M. Generalized Gradient Approximation Made Simple. *Phys. Rev. Lett.* **1996**, *77*, 3865–3868.

(56) Grimme, S.; Antony, J.; Ehrlich, S.; Krieg, H. A Consistent and Accurate Ab Initio Parametrization of Density Functional Dispersion Correction (DFT-D) for the 94 Elements H-Pu. *J. Chem. Phys.* **2010**, *132*, 154104.

(57) Grimme, S.; Ehrlich, S.; Goerigk, L. Effect of the Damping Function in Dispersion Corrected Density Functional Theory. *J. Comput. Chem.* **2011**, *32*, 1456–1465.

(58) Blöchl, P. E. Projector Augmented-Wave Method. *Phys. Rev. B* **1994**, *50*, 17953–17979.

(59) Kresse, G.; Joubert, D. From Ultrasoft Pseudopotentials to the Projector Augmented-Wave Method. *Phys. Rev. B* **1999**, *59*, 1758–1775.

(60) Mathew, K.; Sundararaman, R.; Letchworth-Weaver, K.; Arias, T. A.; Hennig, R. G. Implicit Solvation Model for Density-Functional Study of Nanocrystal Surfaces and Reaction Pathways. *J. Chem. Phys.* **2014**, *140*, 084106.

(61) Mathew, K.; Kolluru, V. S. C.; Mula, S.; Steinmann, S. N.; Hennig, R. G. Implicit Self-Consistent Electrolyte Model in Plane-Wave Density-Functional Theory. *J. Chem. Phys.* **2019**, *151*, 234101.

(62) Hall, D. S.; Self, J.; Dahn, J. R. Dielectric Constants for Quantum Chemistry and Li-Ion Batteries: Solvent Blends of Ethylene Carbonate and Ethyl Methyl Carbonate. *J. Phys. Chem. C* **2015**, *119*, 22322–22330.

(63) Giordano, L.; Akkiraju, K.; Jacobs, R.; Vivona, D.; Morgan, D.; Shao-Horn, Y. Electronic Structure-Based Descriptors for Oxide Properties and Functions. *Acc. Chem. Res.* **2022**, *55*, 298–308.

(64) Levin, E. E.; Vassiliev, S. Yu.; Nikitina, V. A. Solvent Effect on the Kinetics of Lithium Ion Intercalation into $LiCoO_2$. *Electrochim. Acta* **2017**, *228*, 114–124.

(65) Yamada, I.; Iriyama, Y.; Abe, T.; Ogumi, Z. Lithium-Ion Transfer on a Li_xCoO_2 Thin Film Electrode Prepared by Pulsed Laser Deposition—Effect of Orientation-. *Journal of Power Sources* **2007**, *172*, 933–937.

(66) Mortensen, J. J.; Hansen, L. B.; Jacobsen, K. W. Real-Space Grid Implementation of the Projector Augmented Wave Method. *Phys. Rev. B* **2005**, *71*, 035109.

(67) Enkovaara, J.; Rostgaard, C.; Mortensen, J. J.; Chen, J.; Dułak, M.; Ferrighi, L.; Gavnholt, J.; Glinsvad, C.; Haikola, V.; Hansen, H. A.; Kristoffersen, H. H.; Kuisma, M.; Larsen, A. H.; Lehtovaara, L.; Ljungberg, M.; Lopez-Acevedo, O.; Moses, P. G.; Ojanen, J.; Olsen, T.; Petzold, V.; Romero, N. A.; Stausholm-Møller, J.; Strange, M.; Tritsaris, G. A.; Vanin, M.; Walter, M.; Hammer, B.; Häkkinen, H.; Madsen, G. K. H.; Nieminen, R. M.; Nørskov, J. K.; Puska, M.; Rantala, T. T.; Schiøtz, J.; Thygesen, K. S.; Jacobsen, K. W. Electronic Structure Calculations with GPAW: A Real-Space Implementation of the Projector Augmented-Wave Method. *J. Phys.: Condens. Matter* **2010**, *22*, 253202.

(68) Ménétrier, M.; Saadoune, I.; Levasseur, S.; Delmas, C. The Insulator-Metal Transition upon Lithium Deintercalation from $LiCoO_2$: Electronic Properties and ^7Li NMR Study. *J. Mater. Chem.* **1999**, *9*, 1135–1140.

(69) Ménétrier, M.; Carlier, D.; Blangero, M.; Delmas, C. On "Really" Stoichiometric $LiCoO_2$. *Electrochem. Solid-State Lett.* **2008**, *11*, A179.

(70) Leontyev, I. V.; Basilevsky, M. V.; Newton, M. D. Theory and Computation of Electron Transfer Reorganization Energies with Continuum and Molecular Solvent Models. *Theor. Chem. Acc.* **2004**, *111*, 110–121.

(71) Ghosh, S.; Horvath, S.; Soudackov, A. V.; Hammes-Schiffer, S. Electrochemical Solvent Reorganization Energies in the Framework of the Polarizable Continuum Model. *J. Chem. Theory Comput.* **2014**, *10*, 2091–2102.

(72) Liu, L.; Miao, L.; Li, L.; Li, F.; Lu, Y.; Shang, Z.; Chen, J. Molecular Electrostatic Potential: A New Tool to Predict the Lithiation Process of Organic Battery Materials. *J. Phys. Chem. Lett.* **2018**, *9*, 3573–3579.

(73) Choe, Y.-S.; Han, S.-B.; Ahn, J.-H.; Kim, C.-I. An Electrostatic Potential Study of $LiFePO_4$ Cathode Material for Lithium-Ion Battery. *Solid State Commun.* **2021**, *328*, 114231.

(74) Stenlid, J. H.; Johannes Johansson, A.; Brinck, T. The Local Electron Attachment Energy and the Electrostatic Potential as Descriptors of Surface–Adsorbate Interactions. *Phys. Chem. Chem. Phys.* **2019**, *21*, 17001–17009.

(75) Okumura, T.; Shikano, M.; Kobayashi, H. Contribution of Oxygen Partial Density of State on Lithium Intercalation/de-Intercalation Process in $Li_xNi_{0.5}Mn_{1.5}O_4$ Spinel Oxides. *J. Power Sources* **2013**, *244*, 544–547.

(76) Dixit, M.; Markovsky, B.; Schipper, F.; Aurbach, D.; Major, D. T. Origin of Structural Degradation During Cycling and Low Thermal Stability of Ni-Rich Layered Transition Metal-Based Electrode Materials. *J. Phys. Chem. C* **2017**, *121*, 22628–22636.

(77) Comer, B. M.; Li, J.; Abild-Pedersen, F.; Bajdich, M.; Winther, K. T. Unraveling Electronic Trends in O* and OH* Surface Adsorption in the MO_2 Transition-Metal Oxide Series. *J. Phys. Chem. C* **2022**, *126*, 7903–7909.

(78) Kim, S. C.; Kong, X.; Vilá, R. A.; Huang, W.; Chen, Y.; Boyle, D. T.; Yu, Z.; Wang, H.; Bao, Z.; Qin, J.; Cui, Y. Potentiometric Measurement to Probe Solvation Energy and Its Correlation to Lithium Battery Cyclability. *J. Am. Chem. Soc.* **2021**, *143*, 10301–10308.

(79) Wu, Y.; Hu, Q.; Liang, H.; Wang, A.; Xu, H.; Wang, L.; He, X. Electrostatic Potential as Solvent Descriptor to Enable Rational Electrolyte Design for Lithium Batteries. *Advanced Energy Materials* **2023**, *13*, 2300259.

(80) Hafizi, R.; Elsner, J.; Blumberger, J. Ultrafast Electronic Coupling Estimators: Neural Networks versus Physics-Based Approaches. *J. Chem. Theory Comput.* **2023**, *19*, 4232–4242.

(81) Wei, Z.; He, Q.; Zhao, Y. Machine Learning for Battery Research. *J. Power Sources* **2022**, *549*, 232125.

(82) Chen, X.; Liu, X.; Shen, X.; Zhang, Q. Applying Machine Learning to Rechargeable Batteries: From the Microscale to the Macroscale. *Angew. Chem. Int. Ed.* **2021**, *133*, 24558–24570.

(83) Sendek, A. D.; Ransom, B.; Cubuk, E. D.; Pellouchoud, L. A.; Nanda, J.; Reed, E. J. Machine Learning Modeling for Accelerated Battery Materials Design in the Small Data Regime. *Adv. Energy Mater.* **2022**, *12*, 2200553.

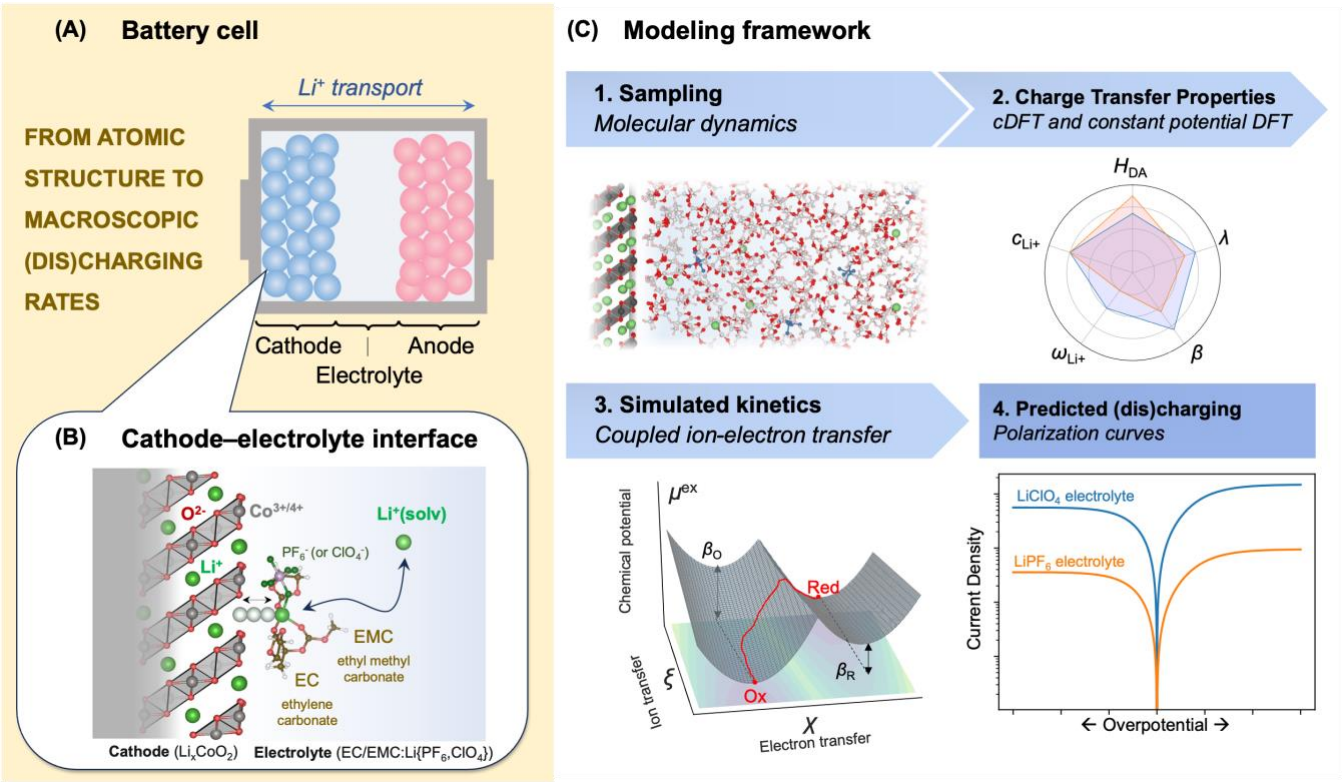

Scheme 1. Interface charge transfer modeling. In (**A**), sketch of a battery cell and (**B**) atomistic image of Li-ion transfer at the Li_xCoO_2(LCO)-electrolyte interface. In this work, 3:7 ethylene carbonate (EC):ethyl methyl carbonate (EMC) electrolytes containing 0.5 M $LiPF_6$ or $LiClO_4$ salts are considered. In (**C**), overview of modeling framework containing four steps: in 1., showing a snapshot of a molecular dynamics simulation of the $Li_{0.5}CoO_2$ interface reproduced with permission from Aggarwal *et al.*[38] ; in 2., example of distribution of charge transfer properties for two electrode-electrolyte interface systems computed with constant potential and constraint DFT; in 3. illustration of theory of coupled ion-electron transfer (CIET) kinetics that evaluates the excess chemical potential of the charge transfer reaction along the electronic (χ) and ionic (ξ) degrees of freedom, readapted from ref.[29] with permission; in 4., example of simulated polarization curve from estimated CIET parameters using the constant potential and constrained DFT (cDFT) modeling framework, as proposed in the current work. Color code in (**B**): Co (grey ●); Li (green ●); O (red ●); C (brown ●); H (white ○); F (dark green ●); F (purple ●).

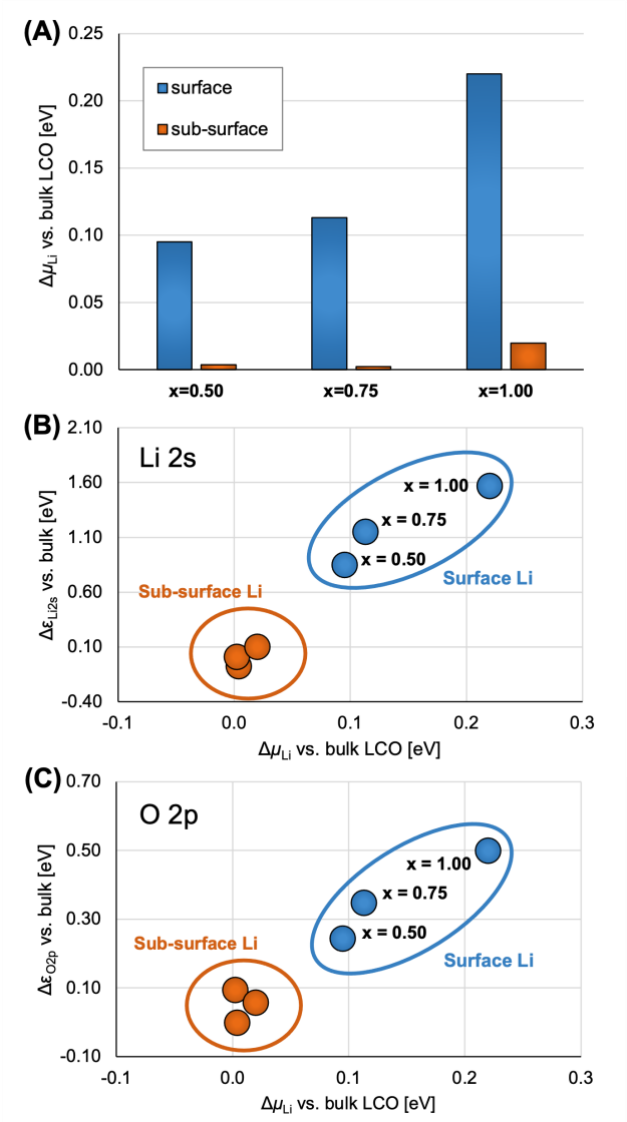

Figure 1. Li defect formation energies. In **(A)**, difference in Li (=Li^++e^-) chemical potential relative to bulk for Li^+ in the surface and subsurface layer of LCO($10\bar{1}4$), respectively. In **(B)**, the difference shift in chemical potential with position is associated with a relative upwards shift in the 2*s*-band center (ε_{Li2s}) of Li in the surface layer, leading to a reduced filling of bonding electronic states. In **(C)**, similar to **(B)** but with the O 2*p*-band center (ε_{O2p}) as descriptor.

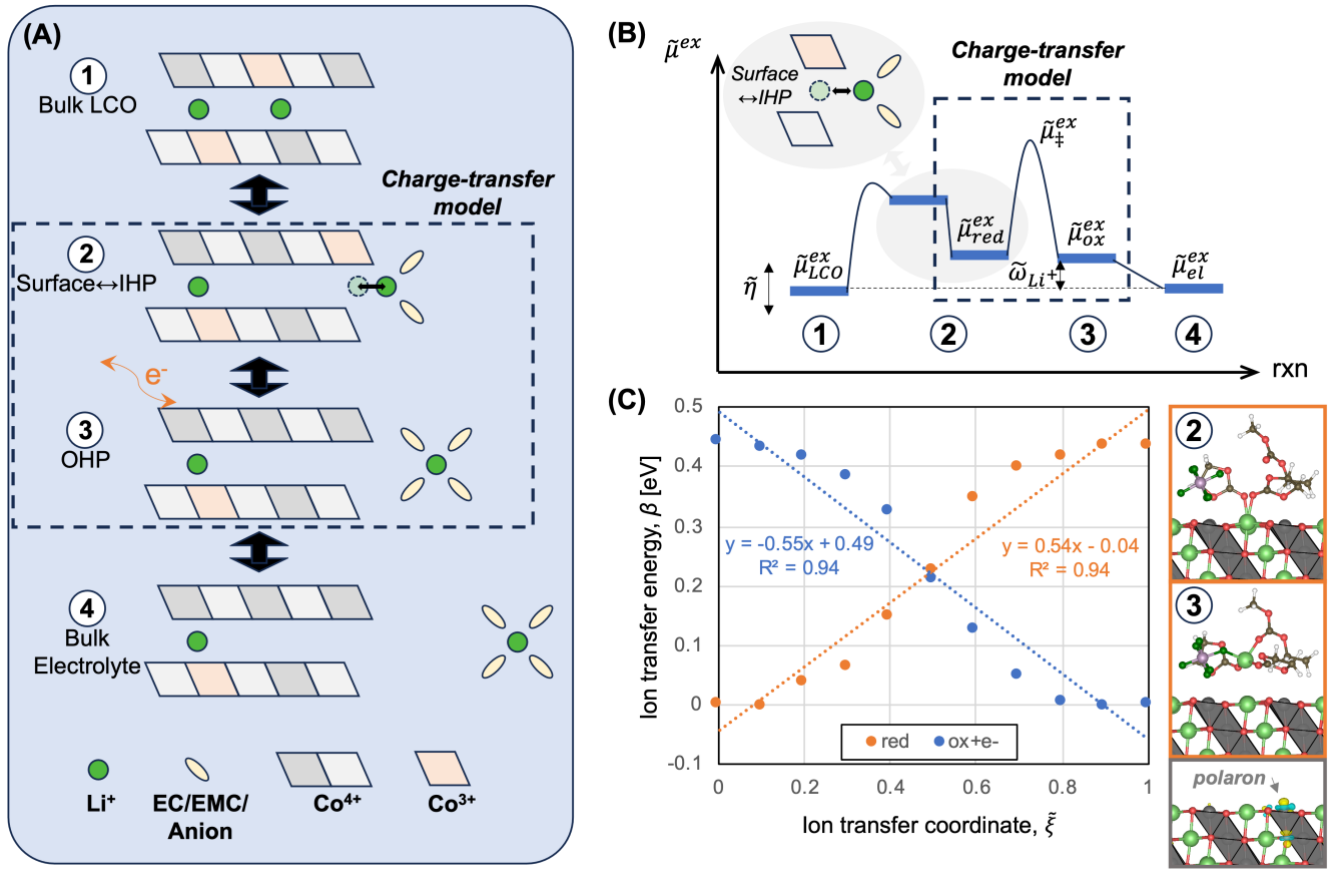

Figure 2. Li-ion transfer mechanism. Schematic of the reversible Li-ion transfer mechanism at the LCO interface in **(A)**. ①→④ corresponding to deintercalation, where intercalated Li^+ (①) journeys via the LCO surface layer (②) to a solvated adsorbed state in the outer Helmholtz plane (③), which is accompanied by oxidation of Co^{3+} to Co^{4+}, before reaching the bulk electrolyte (④). Li^+ prefers protruding ~1 Å from its original lattice position in the surface state (②) under OCV so that Li^+ resides in the inner Helmholtz plane (IHP). In **(B)**, excess chemical potential ($\tilde{\mu}^{ex}$) diagram along reaction coordinate (i.e., joint IT-ET coordinate) for Li^+ transfer with the dotted box indicating the states explicitly treated by the CIET-DFT charge transfer model. In **(C)**, desorption profiles for the lowest energy adsorption state in $LiPF_6$ electrolyte for the reduced (orange) and oxidized (blue) charge states. See **Figure S9** for a corresponding example for $LiClO_4$. The inserts in **(C)** show examples inner (IHP) and outer (OHP) Helmholtz plane solvation structures for Li^+ in the reduced charge state and in $LiPF_6$-electrolyte, as well as an example of the localized polaron state. Color code: Co (grey ●); Li (green ●); O (red ●); C (brown ●); H (white ○); F (dark green ●); F (purple ●).

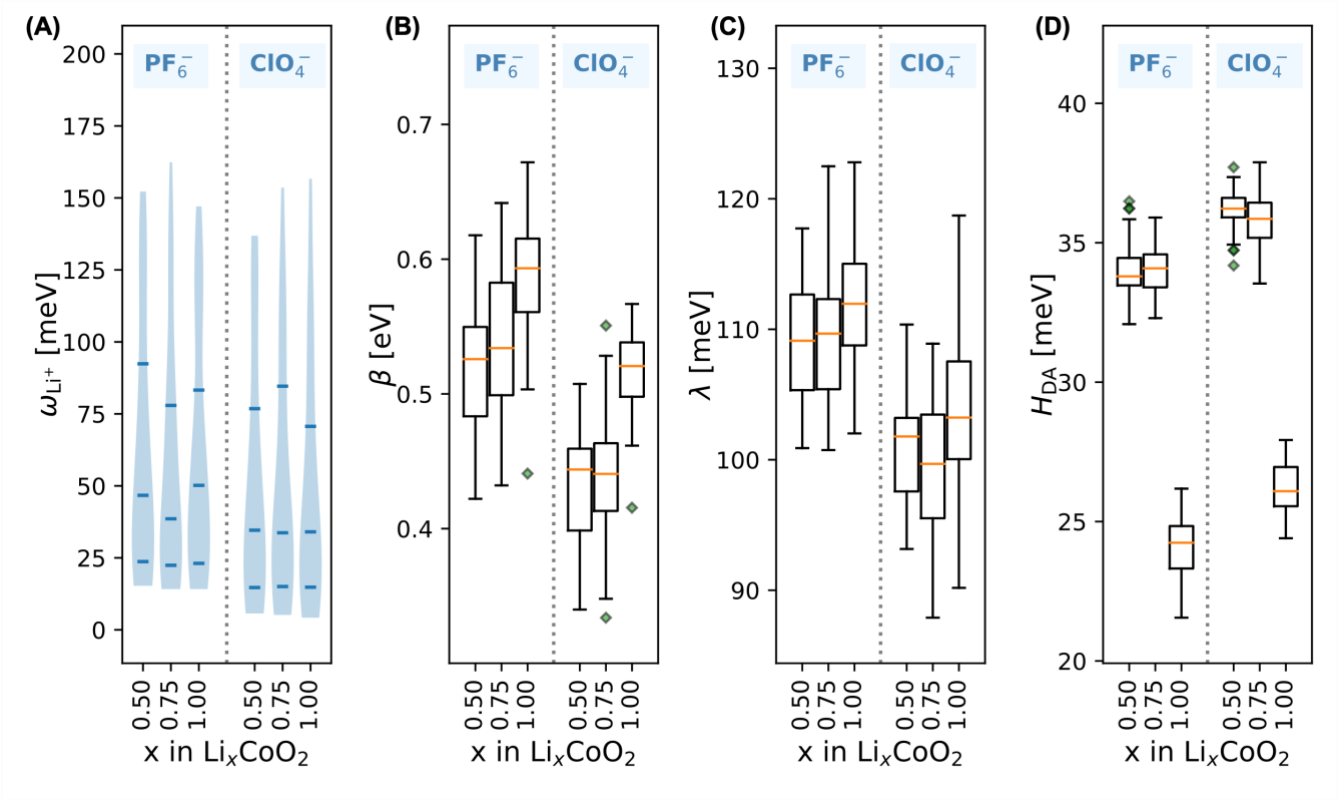

Figure 3. Computed charge transfer parameters. DFT-estimated values for the ω_{Li+}, β, λ, and H_{DA} of different Li^+ coordination complexes adsorbed onto the surface of Li_xCoO_2, x={0.50,0.75,1.00}. Distribution in ω_{Li+} is shown in (**A**) as a violin plot with (from the bottom) the 1st quartile, median, and 3rd quartile marked by horizontal lines. In (B), the average $\beta = \frac{1}{2}[\beta_O + \beta_R]$ is plotted.

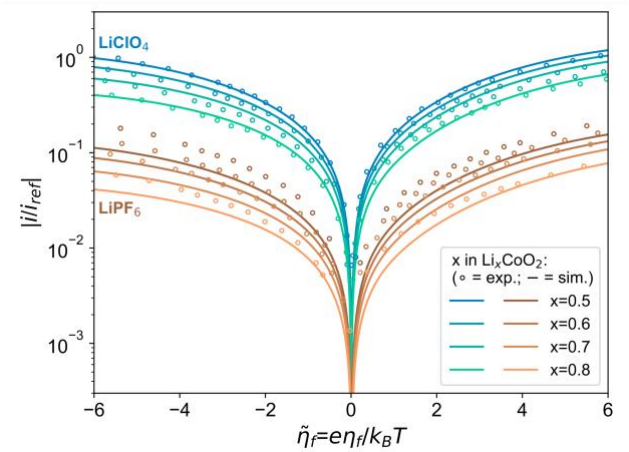

Figure 4. Interface charge-transfer polarization curves. Simulated (sim.) data obtained using the CIET theory in 0.5 M EC/EMC 3:7 electrolytes at 298 K based on the DFT-computed interface properties in **Figure 3**. $|\tilde{\eta}_f|$=6 corresponds to a formal overpotential, η_f, of 0.155 V. Experimental (exp.) data from Zhang *et al.*[27] **Figure S10** includes the same data plotted on a linear scale indicating a relative error of the simulated data within 15% of experimental. On an absolute scale, the simulated data is within one order of magnitude compared to experimental data. Note that the current densities, *i*, are normalized by the reference current density, i_{ref}, corresponding to *i* at $\tilde{\eta}_f$=-6 of $Li_{0.5}CoO_2$ in $LiClO_4$ for the simulated and experimental series, respectively.